Mechanistic Investigations of an α-Aminoarylation Photoredox Reaction

Bernard G. Stevenson, Ethan H. Spielvogel, Emily A. Loiaconi, Victor Wambua, Roman V. Nakhamiyayev, John R. Swierk[*]

Department of Chemistry, State University of New York at Binghamton, Vestal, NY 13850

ABSTRACT: While photoredox catalysis continues to transform modern synthetic chemistry, detailed mechanistic studies involving direct observation of reaction intermediates and rate constants are rare. Using a combination of steady state photochemical measurements, transient laser spectroscopy, and electrochemical methods we rigorously characterize an α-aminoarylation mechanism that is the inspiration for a large number of photoredox reactions. Despite high product yields, the external quantum yield of the reaction remains low (15-30%). Using transient absorption spectroscopy, productive and unproductive reaction pathways were identified and rate constants assigned to develop a comprehensive mechanistic picture of the reaction. The role of the cyanoarene, 1,4-dicyanobenzne, was found to be unexpectedly complex, functioning both as initial proton acceptor in the reaction and as neutral stabilizer for a 1,4-dicyanobenzene radical anion. Finally, we utilize kinetic modeling to analyze the reaction at an unprecedented level of understanding. This modeling demonstrates that the reaction is limited not by the kinetics of the individual steps but instead by scattering losses and parasitic absorption by a photochemically inactive donor-acceptor complex.

INTRODUCTION.

Photoredox catalysis allows for the activation of highly stable bonds by utilizing visible light. Since the first simultaneous reports of photoredox from MacMillan[1] and Yoon,[2] the scope of photoredox reactions has expanded greatly.[3-7] Yet while the development of photoredox methods has accelerated at a remarkable pace, a comprehensive mechanistic understanding has lagged behind. Most reports offer varying degree mechanistic insights through a combination of Stern-Volmer measurements, redox potential measurements, bond dissociation energies, and variation in reagent concentration. [8-11] While this can give information about the initial steps in the reaction, subsequent steps are less well characterized. A complete mechanistic understanding involves direct knowledge of intermediates as well as the kinetics of the productive and unproductive steps. This information can then be used to improve the reaction yields and reaction completion times.[12,13]

Despite a wide variation in the reaction substrates and ancillary reagents, all photoredox methods rely on a photocatalyst to absorb light and initiate the reaction. This photocatalyst is often an organometallic complex with long-lived excited states, though there are many examples using purely organic photocatalysts.[8,14,15] Once a photon is absorbed, the excited state of the photocatalyst can function as either a potent oxidant or reductant, which allows the photocatalyst to generate high energy intermediates that are difficult to achieve thermally.[16] Typically, photoredox reactions proceed via single electron transfer (SET) to a target substrate, which then generates one or more radical species involved in the bond-forming step. Examples of photoredox reactions involving energy transfer instead of electron transfer are also known.[4] Importantly, visible light allows reactions to occur without the use of harsh reaction conditions or reagents that are classically used in synthetic transformations.[17]

While mechanistic information about the initial steps of photoredox reactions is common, complete characterizations of reaction mechanisms and kinetics are rare. Nocera and coworkers used a combination of spectroscopic, electrochemical, and computational methods to fully characterize the catalytic cycle and rate constants of a hydroamidation reaction and with that information improve low quantum yields.[12] Orr-Ewing and coworkers were able to determine the rate constants for electron transfer (ET) and radi-

cal propagation steps for an atom transfer radical polymerization using transient IR techniques.[18,19] Romero and Nicewicz characterized an alkene hydrofunctionalization reaction, observing transient radical intermediates and kinetic information related to a hydrogen atom transfer cycle.[20] Martinez-Haya and coworkers evaluated both the thermodynamics and kinetics for the reductive dehalogenation of several brominated substrates using riboflavin, finding that good agreement between thermodynamic predictions and measured rate constants.[21] Several other groups have utilized transient absorption spectroscopy to observe reaction intermediates in photoredox reactions.[22-30]

α-arylamines and substituted nitrogen heterocycles are important structural motifs in medicinal and pharmaceutical chemistry.[31,35] Generation of these motifs using latent sp^3 C–H bonds via cross-coupling of amines and aryl building blocks has attracted significant attention,[32,33] with photoredox reactions representing a particularly attractive approach.[34] The pioneering work on the photoredox generation of α-arylamines was first reported by MacMillan and coworkers,[35] though the use of electron-deficient arenes and α-amino radicals was subsequently generalized for a host of other photoredox transformations[36-44] and more recently to electrosynthetic chemistry.[45] All of these reactions build on the mechanism first proposed by MacMillan[35] using a prototypical coupling of 1,4-dicyanobenzene (DCB) and N-phenylpyrrolidine (NPP) to generate 4-(1-phenyl-2-pyrrolidinyl)benzonitrile (Scheme 1). On the basis of Stern-Volmer emission quenching studies, redox potentials, and bond dissociation energies, they proposed that upon excitation of an iridium photocatalyst an electron is transferred to DCB to generate a radical anion (DCB•–) and Ir(IV) species. The Ir(IV) species subsequently oxidizes NPP to generate the NPP radical cation (NPP•+) and regenerate the ground state photocatalyst. In their mechanistic proposal, this NPP radical cation is then deprotonated by sodium acetate to give the neutral NPP radical (NPP•), which couples with DCB•– to form the target product.

Scheme 1. α-aminoarylation reaction scheme.
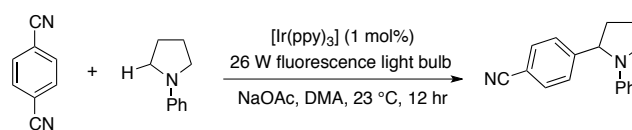
Despite the importance α-arylamines and related photoredox reactions, the reaction mechanism and kinetics are not well characterized. Recently, Walker and coworkers examined the coupling of DCB and various substituted piperidines.[46] In that work they determined the rate constant for back electron transfer between $DCB^{•-}$ and $[Ir(ppy)_3]^+$, as well as the rate constant for the oxidation of the piperidine by $[Ir(ppy)_3]^+$, but the kinetics of subsequent steps were left unexplored. In this work, we utilize a combination of reaction quantum yield measurements, transient absorption spectroscopy (TAS), and electrochemistry to characterize productive and unproductive pathways in the catalytic coupling of DCB and NPP and assign rate constants to all steps. These studies reveal a significantly more complex reaction mechanism that previously suspected, specifically in regards to DCB. Kinetic modeling of the reaction indicates that the quantum yield of the reaction is not limited by the kinetics of the reaction but instead by both scattering and parasitic absorption by a photochemically inactive donor/acceptor complex.

METHODS.

Fac-tris(2-phenylpyridine C,N)iridium (III) (Ir(ppy)$_3$), N,N-dimethylactemide (DMA), (4,4'-di-tert-butyl-2,2'-bipyridine)bis(2-phenylpyridine)iridium(III) hexafluorophosphate (Ir(dtbbpy)ppy$_2$), sodium acetate (NaOAc) and 1,4-dicyanobenzene (DCB) were purchased from Sigma Aldrich. N-phenylpyrrolidine (NPP) was purchased from Alfa Aesar and used as received. DMA was dried over molecular sieves and sodium acetate was dried at 100 °C before use. DCB and sodium acetate were also crushed with a mortar and pestle. All other reagents were used as received.

Quantum Yield Measurements. A stirring flea was placed into a screwtop 1 cm pathlength cuvette along with Ir(ppy)$_3$ (2.5 μmol, .005 equiv), DCB (0.5 mmol, 1 equiv), and sodium acetate

(1.0 mmol, 2 equiv). The solvent, DMA (2 mL), was purged for 30 minutes with argon before being added to the cuvette via syringe along with and NPP (1.5 mmol, 3 equiv). The complete solution was then bubbled with argon in the dark for an additional 45 minutes. For reactions that varied in light intensity, the cuvette was placed on a stirring plate with a 3D printed cuvette holder in front of a collimated 415 nm LED (Thor Labs M15LP1) for 1-30 hours. The LED light intensity was measured using a calibrated photodiode (Thor Labs S120C). For wavelength-dependent reactions, the cuvette was placed on a stir plate in front of a 950 W Xe arclamp (Oriel 66921) equipped with a monochromator (Spectral Products CM110) for 2 hours. After illumination, 0.25 mmol of triphenylmethane was added as an internal standard and the reaction allowed to stir for 30 minutes in the dark. 100-200 μL of reaction mixture was then dissolved in d-acetonitrile and the reaction yield calculated with quantitative ^{1}H Nuclear Magnetic Resonance with a Bruker 400MHz NMR. The external quantum yield (QY) was then calculated according to the following equation:

$$\text{Quantum Yield} = \frac{\text{moles of product}}{\text{moles of incident photons}}$$

Transient Absorption Spectroscopy (TAS) Experimentation. Transient absorption experiments were carried out using a Spectra-Physics Quanta-Ray Pro-290 pulsed Nd:YAG laser (10 Hz) fitted with a PrimoScan OPO. An excitation wavelength of 415 nm (900 μJ/cm^2) was used for all experiments. Laser pulses were chopped at every other pulse to improve the signal to noise ratio per the method of Rimshaw et. al.[47] The sample was illuminated with a broadband white light source (Energetiq EQ-99X), with a shutter before the sample to minimize light exposure. After the sample, probe light was collected by a monochromator (Spectral Products DK240) and passed onto a silicon photodiode (ThorLabs DET10A). Data was collected with a Pico Technology 6404C oscilloscope and analyzed using software written in LabView.

Single wavelength traces were collected at 6.4 ns intervals up to 12 μs and at 1μs intervals up to 10 ms. The short-time and long-time data traces were stitched together before fitting. For short-time traces, data was collected with the probe on and off to remove any residual laser scattering. For TAS experiments, solution concentrations of 37 μM Ir(ppy)$_3$, 50 mM DCB, and 150 mM NPP in DMA were used. Solutions were prepared under an argon atmosphere for 90 minutes in a four-sided screw top cuvette with cap and septum before TAS experiments. Samples were changed every two hours with stability confirmed by comparing single wavelength traces at the same wavelength collected at different times throughout the experiment. The TAS traces were fit to a kinetic model described in the supporting information.

Spectrochemical Studies. All spectroelectrochemical experiments were performed using a BioLogic SP-50 potentiostat, a platinum honeycomb spectroelectrochemical cell (Pine) with a pathlength of 1.7 mm, and a Shimadzu UV-2600 UV-Vis Spectrophotometer. Electrochemical potentials were applied relative to a Ag/Ag$^+$ reference electrode. For all spectroelectrochemical studies, 0.1 M tetrabutylammonium hexafluorophosphate (TBAPF$_6$) in DMA was used as the electrolyte. Concentrations of 83 and 590 μM were used for Ir(ppy)$_3$ and DCB, respectively. Spectroelectrochemical studies of NPP failed to produce a stable spectrum for the radical cation and were not pursued.
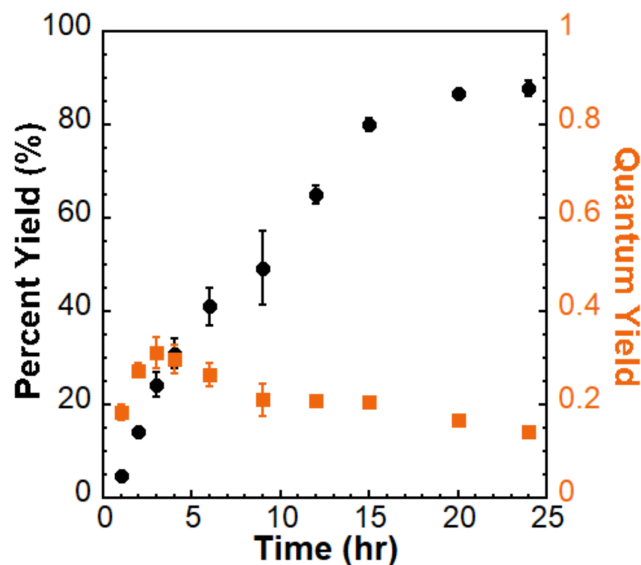
RESULTS AND DISCUSSION

Quantum yield measurements. At an excitation wavelength of 415 nm, we observed QY in the range of 0.15-0.3 (Figure 1), depending on the length of the reaction, which is consistent with the α-arylation reaction not proceeding through a radical chain pathway. After 24 hours, the reaction reached a maximum percent yield of 88% when measured by quantitative NMR (Figure S1 and S2) and was independent of wavelength (Figure S3). We also observed that the reaction rate was the same at high (10.4 mW) and low (5.06 mW, Figure S4) light intensities when normalized for photon flux.

A reaction quantum yield of 0.15-0.3 is in good agreement with other studies on non-radical chain propagation reactions, where typical quan-

tum yields of photoredox reactions can range from .19 to .43.[48–50] Ellman and coworkers partly explored the mechanism of a closely related α-amino arylation reaction involving substituted piperidine analogues and observed 0.4-0.6 at early timescales,[46] which is in relatively good agreement with our quantum yields. These results were collected without the use of insoluble sodium acetate, which actinometry experiments suggest scatter 10-20% of incoming photons.

Over the course of the reaction, the QY shows significant variation. We assign the gradual decrease in QY from 3+ hours to the formation of acetic acid. NMR data (Figure S5) shows that acetic acid is formed from sodium acetate over the course of the reaction (*vide infra*), which eventually competes with DCB as an electron acceptor for the excited photocatalyst. We determined a quenching rate constant for acetic acid of 5.8×10^8 M^{-1} s^{-1}, which is comparable to the quenching rate constant for DCB (2.2×10^9 M^{-1} s^{-1}). Furthermore, TAS data demonstrates that in the presence of excess acetic acid, charge transfer to DCB does not occur (Figure S6).

The cause of the increase in QY over the first three hours is less clear, though we suggest it is related to a decrease in scattering by sodium acetate. We hypothesize that as sodium acetate is converted to acetic acid, the particle size decreases as does scattering, which leads to an increase in QY. By comparison, when the soluble base

tetrabutylammonium acetate is used, the QY is ~52% at 30 min and then decreases to 42% at one hour.

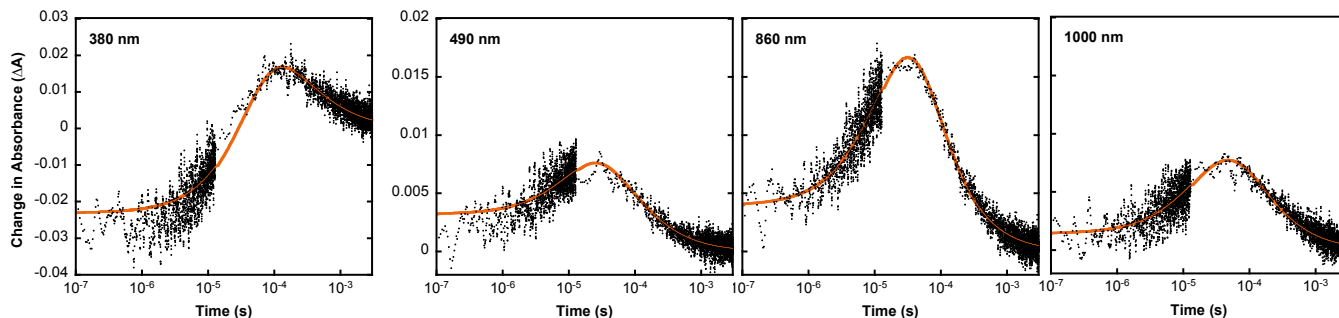**Electron transfer between DCB and Ir(ppy)$_3$.** We collected TAS data from 100 ns to 10 ms and from 340 to 1100 nm (Figure 2) to examine the rate at which the DCB radical anion can undergo back electron transfer (BET) with Ir(IV). Initially in the TAS spectrum there are positive absorption features at wavelengths longer than 460 nm and a bleach centered at 380 nm. Both are consistent with the formation of Ir(IV) (Figure S7). There is also a new absorption at ~430 nm that we assign to the DCB radical anion (Figure S8). At 100 ns, the transient spectrum could be reproduced by
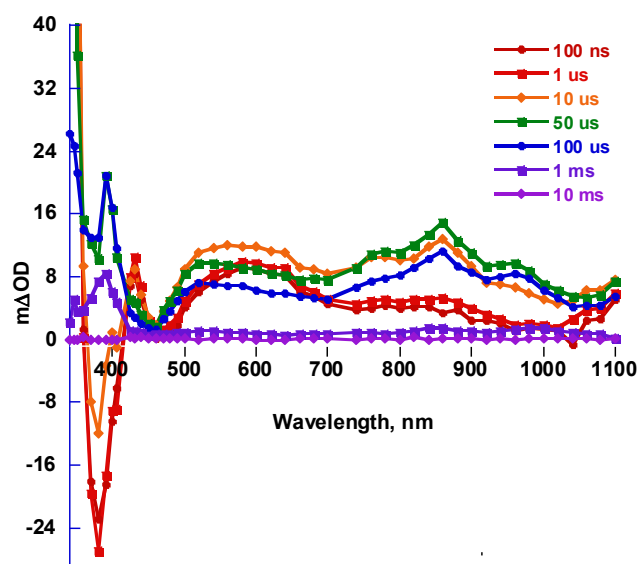
Figure 2. Transient absorption spectrum of 37μM Ir(ppy)$_3$ and 50mM DCB at 415nm excitation from 100ns to 10ms.

combining the difference spectra obtained from the spectroelectrochemical spectrum for [Ir(ppy)$_3$]$^+$ and DCB$^{•-}$. From this, we determine an initial concentration of 3.55 μM for both species (Figure S9).

Unexpectedly, at longer times (>1 μs) we see changes in the transient spectra that are consistent with the formation of a new species. Most notably, a new absorption at ~860 nm forms on a tens of microseconds timescale that cannot be assigned to either [Ir(ppy)$_3$]$^+$ or DCB•−. In addition, the bleach at 380 nm is replaced by a new absorption, and the absorption at 600 nm blueshifts and changes shape. We assign these new absorbances to the formation of new species, which we formulate as (DCB)$_2^{•-}$. Increasing the


Figure 1. Percent yield (black circles) and external quantum yield (orange squares) of reaction illuminated by a 415 nm LED. (10.4 mW cm^{-2})

Figure 3. Single wavelength traces of 3.7 µMIr(ppy)3, 50 mM DCB at 360nm, 620nm, and 860 nm at 415 nm excitation (0.9 mJ/cm^2 per pulse, gray). Orange line is fit to kinetic model.

concentration of DCB while maintaining a constant pump fluence leads to a larger change in absorbance (Figure S10). Fits of single wavelength traces at different concentrations demonstrate a second order reaction dependence on the concentration of DCB•– and neutral DCB and all concentrations can be fit using the same set of kinetic parameters. In addition, spectroelectrochemistry at high concentrations of DCB reveal an absorption feature that peaks at 860 nm and is not present at lower concentrations of DCB (Figure S11). While further studies are planned to elucidate the nature of this intermediate, previous work demonstrates that the solution chemistry of cyanoarene radical anions can involve multiple species, including dimers.[51]
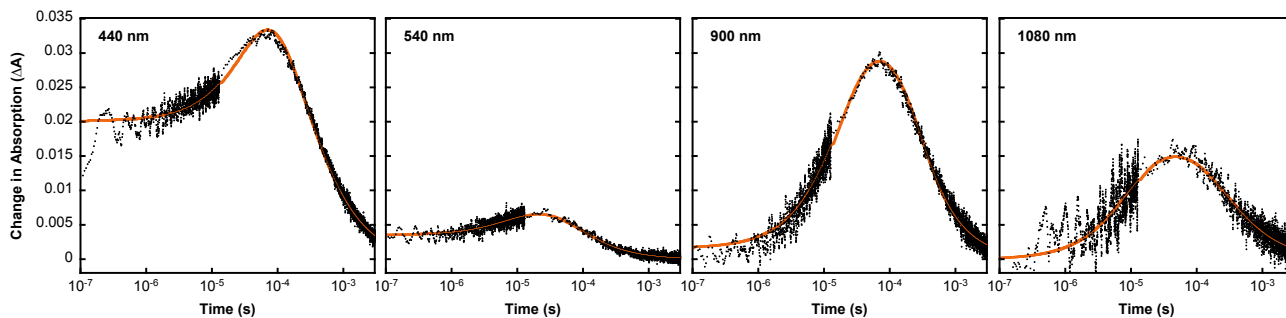
In order to understand the kinetics of electron transfer between Ir(ppy)$_3$, DCB, and (DCB)$_2$•– we developed a kinetic model that incorporates back electron transfer between Ir(IV) and DCB$^•-$ (k_{recomb}), pairing of DCB•– and DCB (k_{pair}), and electron transfer between Ir(IV) and (DCB)$_2^{•-}$ ($k_{recomb2}$) and applied it to the single wavelength absorption traces (Figure 3, Table S1). We calculated an average rate constant for recombination, k_{recomb}, of 5.4(±0.7) x 10^9 M^{-1} s^{-1}. Though this recombination is nearly diffusion controlled, the low concentration of Ir(IV) and DCB$^•-$ mean it is not the dominant pathway. Instead, the model suggests that DCB•– forms (DCB)$_2$•– with a rate constant of 1.1(±0.1) x 10^6 M^{-1} s^{-1}. Back electron transfer then occurs between (DCB$_2$)$^{•-}$ and Ir(IV) ($k_{recomb2}$ = 6.0(± 0.6) x 10^9 M^{-1} s^{-1}. The absorption spectrum for (DCB)$_2$•– was determined from these fits (Figure S12).

Electron transfer between DCB, NPP, and Ir(ppy)$_3$. Following our TAS studies with only

DCB and Ir(ppy)$_3$, we then included NPP. It is immediately obvious that the transient spectra are remarkably different with NPP added (Figure 4). On short timescales (< 10 µs) there is a broad absorbance from 400-600nm with a sharp peak at 440 nm. There is also a slight increase in absorption in the near-IR. We assign the broad 400-600 nm absorption to the formation of NPP•+ (Figures S13) and the peak at 440 nm to DCB•–. We do not see any features that we can assign to [Ir(ppy)$_3$]$^+$, which suggests that oxidation of NPP is complete within 100 ns. While this precludes us from making a definitive assignment for the rate constant of oxidation, k_{ox}, we can use kinetic modeling to estimate a minimum value of k_{ox} as 4 x 10^8 M^{-1} s^{-1}. From fitting the transient spectrum at 100 ns, we estimate an initial concentration of 3.1 µM of DCB•– and NPP•+ (Figure S14). Though the pump fluence is constant, this de-
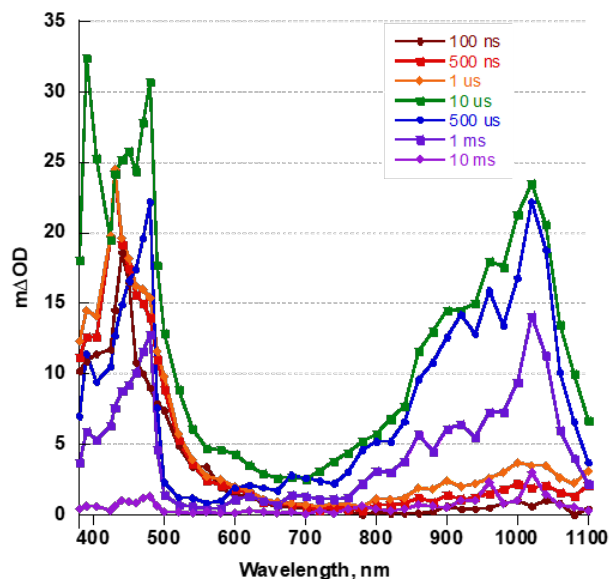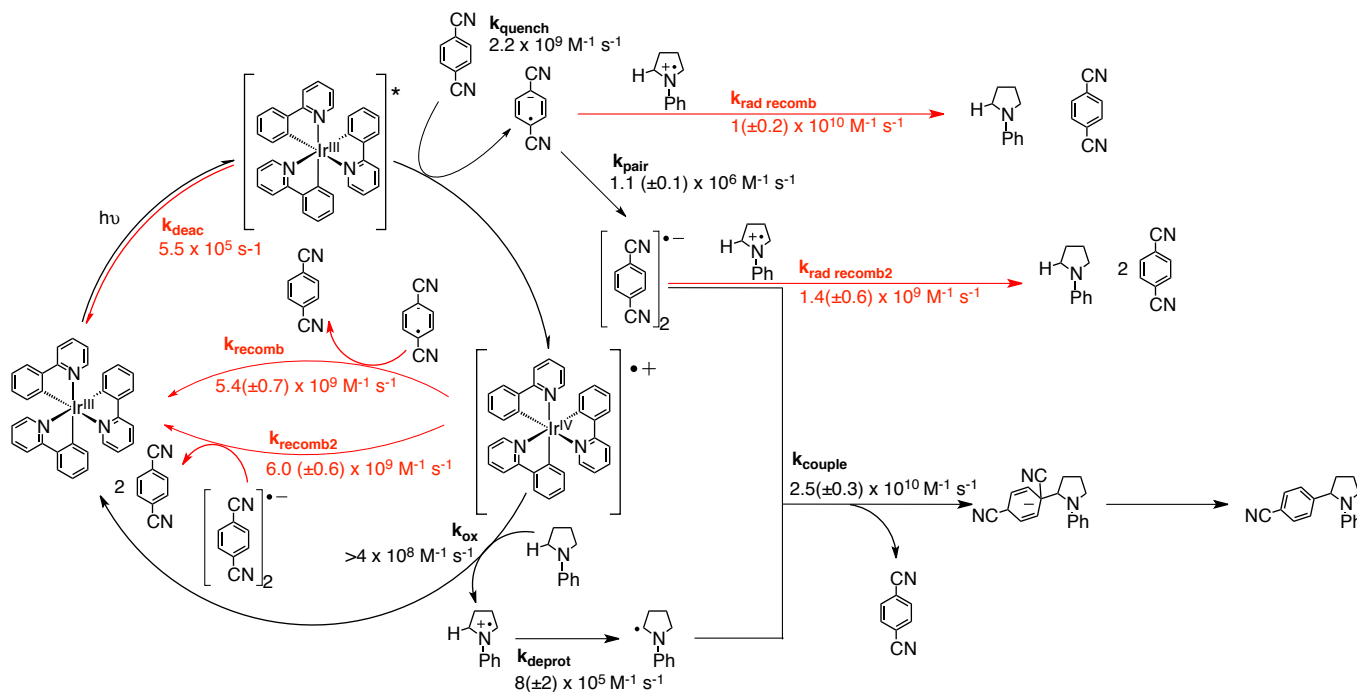

Figure 4. Transient Absorption Spectrum of 37 µM Ir(ppy)$_3$, 50 mM DCB, and 150 mM NPP at 415 nm excitation from 100 ns to 10 ms.

Figure 5. Single wavelength traces of 3.7 μM Ir(ppy)3, 50 mM DCB, and 150 mM NPP at 540nm, 800nm, and 900 nm at 415 nm excitation (0.9 mJ/cm^2 per pulse, gray). Orange line is fit to kinetic model.

crease in the concentration of charge separated species is likely due to formation of a photochemically inactive donor acceptor complex between DCB and NPP that parasitically absorbs at 415 nm (Figure S15) but does not exhibit any photochemical response in the TAS. Also, illumination of the reaction with Ir(ppy)3 also does not result in product formation.

At 10 μs and longer, the transient spectra change dramatically. Most notably a large transient absorption develops in the near IR from 700 to 1100 nm, as well as an increase in the absorption between 400 and 600 nm. While to the best of our knowledge the absorption spectrum for NPP• is not available, these absorption features are generally consistent with alkane radicals.[52,53]

Direct oxidation of NPP with Ir(tbbpy)(ppy)2 generates the same species (Figure S16)

Single wavelengths traces (Figure 5) confirm the formation of a new species on a 10-100 μs timescale, followed by decay over milliseconds. We could not fit these traces using a simple exponential model, so we expanded the kinetic model used in the Ir(ppy)3/DCB experiments to include deprotonation of NPP$^{•+}$, k_{deprot}, and coupling of NPP$^{•}$ and (DCB)$_2$$^{•-}$, k_{couple}. Though we also initially included coupling between NPP•+ and DCB•−, the curve fitting consistently set this the rate constant for this coupling to zero, indicating that DCB•− does not undergo coupling. Also, while not included in the original mechanistic proposal,[35] we found that the data could not be fit

Figure 6. Overall kinetic scheme with rate constants for the coupling of N-phenylpyrrolidine (NPP) and 1,4-dicyanobenzene (DCB). Red arrows indicate steps that are catalytically unproductive.

unless we included terms that described unproductive electron transfer between NPP•+ and DCB•−, $k_{rad\ recomb}$, and $(DCB)_2$•−, $k_{rad\ reccomb2}$, which results in the regeneration of DCB and NPP. Using our expanded model, we were able to fit the TAS traces and extract rate constants (Figure 6, Table S2).

The kinetic scheme in Figure 6 reveals several key features about this reaction. First, the slowest step is the deprotonation of NPP•+, which serves as a necessary precursor to coupling. While the reaction is waiting for deprotonation to occur, unproductive electron transfer between the radical ions can occur, leading to a decrease in quantum yield. It is particularly interesting that this unproductive step is nearly an order of magnitude slower with $(DCB)_2{}^{•−}$ than with $DCB^{•−}$. This suggests that pairing stabilizes the radical anion, allowing it to persist until the formation of NPP•. We also note that the rapid oxidation of NPP by Ir(IV) means that back electron transfer to the oxidized photocatalyst plays no role in the complete reaction and demonstrates that electron transfer between radical ions is the primary unproductive step that can limit the reaction.

Role of the base in the reaction. Deprotonation of NPP•+ is the key mechanistic step in the reaction. In the original report it was proposed that sodium acetate is the primary base, however, we suggest that sodium acetate is not the primary proton acceptor from NPP•+. For one, sodium acetate is insoluble in DMA, which would make rapid deprotonation of NPP•+ unlikely. Also, we measured the apparent deprotonation rate of NPP•+ electrochemically and observed no difference in the rate with or without sodium acetate (Figure S17). Lastly, Walker et al. observed that removal of sodium acetate from the coupling of DCB and piperidines had no effect on the reaction.[44] Inclusion of sodium acetate is apparently necessary for the reaction as the maximum percent yield without added base was 37±1% after 48 hours compared to 87% with sodium acetate (Figure S18). Also, NMR of the final reaction mixture shows that acetic acid is generated during the reaction (Figure S5), indicating that sodium acetate is the eventual proton acceptor.

Instead, we suggest that DCB functions as the primary proton acceptor in the reaction and then transfers the proton to sodium acetate on a slower timescale. As noted above, without added base the reaction yield does not exceed 37%. If NPP was the primary proton acceptor, that would correspond to roughly 14% of the remaining NPP being protonated, while if DCB was the primary proton acceptor then 60% of the remaining DCB would be protonated. This is consistent with our NMR data for the no sodium acetate reaction. While the percent yield is 37%, the conversion of DCB is 99% (Figure S19 and S20), indicating that DCB is being consumed via some other pathway. We suggest this pathway is functioning as a base to deprotonate NPP•+. Electrochemical experiments also provide further indication of DCB acting as a base. When DCB is added to a solution of NPP, the anodic peak potential for NPP oxidation shifts to more positive potentials. This suggests that the kinetic control of deprotonation occurs at higher scan rates, outside of our window of measurement, and is consistent with a faster rate of deprotonation.

Kinetic Modeling. Using the values in Figure 6, we developed a kinetic model of the reaction. Under reaction conditions, we determined an internal quantum yield of nearly 1 (Figure 7) at short times (< 1 hr), before decaying over the course of 24 hours due to the generation of acetic acid and depletion of DCB. This means that in the absence of acetic acid nearly all absorbed photons result in product formation. We next calculated the quantum yield based on the number
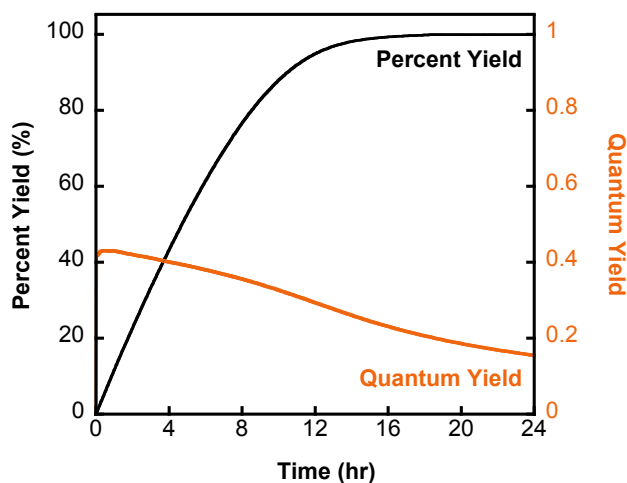
Figure 7. Simulated external quantum and percent yields using the values in Figure 6 and accounting for scattering losses and parasitic absorption by NPP/DCB donor-acceptor complex

of incident photons (i.e., external quantum yield). We first accounted for parasitic absorbance by the DCB/NPP donor-acceptor complex. On the basis of the concentrations of Ir(ppy)$_3$ and DCB/NPP, we estimate that 44.2% of incoming photons are absorbed by the DCB/NPP donor acceptor complex and result in no productive photochemistry. This resulted in a maximum external quantum yield of 0.54, which is excellent agreement with our observations using TBA acetate. Finally, we accounted by scattering by the sodium acetate, which our actinometry experiments estimate at ~20% of incoming photons. This results in a maximum external quantum yield of 0.43, which decays to 0.15 at 24 hours. In general, this is in good agreement with our experimental quantum yield, except at times less than 4 hours where the model overestimates the quantum yield (Figure 7).

Taken together, the modeling demonstrates that the limitations on this reaction are not related to the coupling chemistry but to scattering losses and parasitic absorption by the NPP/DCB donor acceptor complex. The latter is particularly problematic as increasing the concentration of photocatalyst will have little impact on the partition of photons between the photocatalyst and donor acceptor complex. Likewise, decreasing the concentration of NPP and DCB lead to a decrease in the overall quantum yield as well. Decreasing the concentration of NPP and DCB to 150 and 50 mM, respectively, leads to a maximum internal quantum yield of 89%. At lower concentrations, unproductive pathways can better compete with productive pathways and lead to a decrease in quantum yield.

Interestingly, variation of the different rate constants reveals that there is a significant amount of kinetic redundancy in this reaction. For example, we predict that the oxidation of NPP by Ir(IV) can be slowed by several orders of magnitude without having an impact on the reaction. (Figure S21). Likewise, the rate of deprotonation of NPP•+ or quenching of Ir(ppy)$_3$* could both be slowed by more than an order of magnitude without impacting the quantum yield (Figures S22 and S23). Unproductive pathways (e.g., radical recombination) would need to be significantly faster than diffusion-controlled to impact the quantum yield of the reaction. These observa-

tions may explain the quantum yield results reported by Walker et al.[44] for the coupling of 2-methyl-1-phenylpiperidine with DCB (0.4-0.6). In that study, the authors report that oxidation of the piperidine, k_{ox}, is at least one magnitude slower (2.4 x 10^7 M^{-1}s^{-1}) than what we observe (>4 x 10^8 M^{-1}s^{-1}). This difference in rate is likely related to the presence of a methyl group adjacent to the amine nitrogen. Our kinetic modeling suggests that k_{ox} can be as slow as 10^5 M^{-1} s^{-1} without having a significant impact on the overall quantum yield. Assuming the formation of a similarly absorbing donor/acceptor species between the DCB and 2-methyl-1-phenylpiperidine, a QY of 0.4-0.6 would correspond to an internal quantum yield near to 1.

CONCLUSION.

Through a combination of steady state photochemical measurements, laser spectroscopy, and electrochemical methods we have rigorously characterized a photoredox reaction that is broadly relevant to wide range of transformations. While the overall yield of the reaction is high, the external quantum yield of the reaction is more modest, only 0.15 to 0.3 depending on the length of the reaction. Characterization of the rate constants for productive and unproductive pathways allowed us to develop a kinetic model of this reaction. Unlike previous mechanistic studies of photoredox reactions, we are able to use this model to predict reaction behavior in good agreement with experimental results.

The kinetic modeling demonstrates that nearly all photons that are absorbed by Ir(ppy)$_3$ result in product formation. We observe an experimental quantum yield of much less than 1 because scattering and parasitic photon absorption prevent ~57% of the incoming photons from reaching Ir(ppy)$_3$. While scattering can be overcome by using a soluble base, the formation of the NPP/DCB donor-acceptor complex provides a unique challenge to the reaction. Decreasing the concentration of NPP and/or DCB will reduce the absorbance of the donor-acceptor complex and increase the fraction of photons absorbed by Ir(ppy)$_3$. At the same time, key pathways in the reaction such as reduction of [Ir(ppy)$_3$]$^+$ and deprotonation of NPP•+ rely on high concentrations of NPP and DCB to outcompete unproduc-

tive pathways. Instead, efforts to improve the quantum yield of this reaction should focus on identifying conditions that may disrupt the formation of this donor/acceptor species (e.g., different solvent, inert electrolyte).

Finally, our results also introduce questions about the role of the cyanoarene in this coupling reaction. Not only do we demonstrate the DCB•– pairs with a neutral DCB, but our evidence also suggests that DCB is in fact the primary proton acceptor from NPP•+. However, our model fails to explain why other cyanoarenes do not achieve high product yields.[35] While poor quenching kinetics may result is a low rate of product formation, eventually the percent yield of the reaction should approach 100%. Experiments demonstrate this is not the case outside of DCB, suggesting a yet unknown pathway that leads to an irreversible loss of the cyanoarene. Other cyanoarenes may function as poorer bases than DCB or may undergo decomposition pathways when protonated. Studies are currently underway to understand how the mechanism changes when other cyanoarenes other than DCB are used.

ASSOCIATED CONTENT

Supporting Information

The Supporting Information is available free of charge on the ACS Publications website.

> Detailed procedures for fitting TAS traces, determining the spectra of NPP•+ and NPP•, electrochemical measurement of the apparent deprotonation rate, estimation of scattering losses, and kinetic modeling; NMR data of reaction mixtures; quantum yield as a function of wavelength and light intensity; spectro-electrochemically difference spectra; NMR showing acetic acid formation; TAS data showing impact of acetic on charge separation; spectra of NPP•+, NPP•, and (DCB)₂•–; quantum and percent yield without sodium acetate; percent conversion of DCB without added sodium acetae; simulated rate constant data from kinetic modeling; electrochemical data for the rate of deprotonation. (PDF)

AUTHOR INFORMATION

Corresponding Author

* E-mail: jswierk@binghamton.edu

ACKNOWLEDGMENT

REFERENCES

1. Nicewicz, D. A. and MacMillan, D. W. C. Merging Photoredox Catalysis with Organocatalysis: The Direct Asymmetric Alkylation of Aldehydes. *Science*. **2008**, *322*, 77-80.
2. Ischay, M. A.; Anzovino, M. E.; Du, J.; Yoon, T. P. Efficient Visible Light Photocatalysis of [2+2] Enone Cycloadditions. *J. Am. Chem. Soc.* **2008**, *130*, 12886-12887.
3. Narayanam, J.M.R.; Stephenson, C.R.J. Visible Light Photoredox Catalysis: Applications in Organic Synthesis. *Chem. Soc. Rev.* **2011**, *40*, 102-113.
4. Prier, C. K.; Rankic, D. A.; MacMillan, D. W. C. Visible Light Photoredox Catalysis with Transition Metal Complexes: Applications in Organic Synthesis. *Chem. Rev.* **2013**, *113*, 5322–5363.
5. Romero, N. A.; Nicewicz, D. A. Organic Photoredox Catalysis. *Chem. Rev.* **2016**, *116*, 10075–10166.
6. Yoon, T. Photochemical Stereocontrol Using Tandem Photoredox-Chiral Lewis Acid Catalysis. *Acc. Chem. Res.* **2016**, *49*, 2307-2315.
7. Matsui, J. K.; Lang, S. B.; Heitz, D. R.; Molander, G. A. Photoredox-Mediated Routes to Radicals: the Value of Catalytic Radical Generation in Synthetic Methods Development. *ACS Catalysis* **2017**, *7*, 2563–2575.
8. Arias-Rotonda, D. M.; McCusker, J. K. The Photophysics of Photoredox Catalysis: A Roadmap for Catalyst Design. *Chem. Sci. Rev.* **2016**, *45*, 5803-5820.
9. Pitre, S.P.; McTiernan, C.D.; Scaiano, J.C. Understanding the Kinetics and Spectroscopy of Photoredox Catalysis and Transition-Metal-Free Alternatives. *Acc. Chem. Res.* **2016**, *49*, 1320-1330.
10. Blanksby, S. J.; Ellison, G. B. Bond Dissociation Energies of Organic Molecules. *Acc. Chem. Res.* **2003**, *36*, 255−263.
11. Waidmann, C. R.; Miller, A. J. M.; Ng, C.-W. A.; Scheuermann, M. L.; Porter, T. R.; Tronic, T. A.; Mayer, J. M. Using Combinations of Oxidants and Bases as PCET Reactants: Thermochemical and Practical Considerations. *Energy Environ. Sci.* **2012**, *5*, 7771−7780.
12. Ruccolo, S.; Qin, Y.; Schnedermann, C.; Nocera, D. G. General Strategy for Improving the Quantum Efficiency of Photoredox Hydroamidation Catalysis. *J. Am. Chem. Soc.* **2018**, *140*, 14926-14937.
13. Thompson, W. A.; Fernandez, E. S.; Maroto-Valer, M. M. Review and Analysis of CO₂ Photoreduction Kinetics. *ACS Sustainable Chem. Eng.* **2020**, *8*, 4677-4692.
14. Ravelli, D.; Fagnoni, M. Dyes as Visible Light Photoredox Organocatalysts. *ChemCatChem* **2012**, *4*, 169-171.
15. Larsen, C.B.; Wenger, O.S. Photoredox Catalysis with Metal Complexes Made from Earth-Abundant Elements. *Chem. Eur. J.* **2018**, *24*, 2039-2058.
16. Teegardin, K.; Day, J. I.; Chan, J.; Weaver, J. Advances in Photocatalysis: A Microreview of Visible Light Mediated Ruthenium and Iridium Catalyzed Organic Transformations. *Org. Process. Res. Dev.* **2016**, *20*, 1156-1163.
17. Yoon, T. P. Visible Light Photocatalysis: The Development of Photocatalytic Radical Ion Cycloadditions. *ACS Catal.* **2013**, *3*, 895-902.
18. Koyama, D.; Dale, D.J.A.; Orr-Ewing, A.J. Ultrafast Observation of a Photoredox Reaction Mechanism: Photoinitiation in Organocatalyzed Atom-Transfer Radical Polymerization. *J. Am. Chem. Soc.* **2018**, *140*, 1285-1293.
19. Lewis-Borell, L.; Sneha, M.; Bhattacherjee, A.; Clark, I. P.; Orr-Ewing, A. J. Mapping the Multi-step Mechanism of a Photoredox Catalyzed Atom-Transfer Radical Polymerization Reaction by Direct Observation of the Reactive Intermediates. *Chem. Sci.* **2020**, *11*, 4475-4481.
20. Romero, N.A.; Nicewicz, D.A. Mechanistic Insight into the Photoredox Catalysis of Anti-Markovnikov Alkene Hydrofunctionalization Reactions. *J. Am. Chem. Soc.* **2014**, *136*, 17024-17035.

21. Martinez-Haya, R.; Miranda, M.A.; Marin, M.L. Metal-Free Photocatalytic Reductive Dehalogenation Using Visible-Light: A Time-Resolved Mechanistic Study. *Eur. J. Org. Chem.* **2017**, 2164-2169.

22. Herzog, W.; Bronner, C.; Löffler, S.; He, B.; Kratzert, D.; Stalke, D.; Hauser, A.; Wenger, O.S. Electron Transfer between Hydrogen-Bonded Pyridylphenols and a Photoexcited Rhenium(I) Complex. *ChemPhysChem* **2013**, *14*, 1168-1176.

23. Rueda-Becerril, M.; Mahé, O.; Drouin, M.; Majewski, M.B.; West, J.G.; Wolf, M.O.; Sammis, G.M.; Paquin, J-F. Direct C–F Bond Formation Using Photoredox Catalysis. *J. Am. Chem. Soc.* **2014**, *136*, 2637-2641.

24. Majek, M.; Jacobi von Wangelin, A. Mechanistic Perspectives on Organic Photoredox Catalysis for Aromatic Substitutions. *Acc. Chem. Res.* **2016**, *49*, 2316-2327.

25. Ng, Y.Y.; Tan, L.J.; Ng, S.M.; Chai, Y.T.; Ganguly, R.; Du, Y.; Yeow, E.K.L.; Soo, H.S. Spectroscopic Characterization and Mechanistic Studies on Visible Light Photoredox Carbon-Carbon Bond Formation by Bis(Arylimino)Acenaphthene Copper Photosensitizers. *ACS Catal.* **2018**, *8*(12), 11277-11286.

26. Ma, J.; Zhang, X.; Phillips, D.L. Time-Resolved Spectroscopic Observation and Characterization of Water-Assisted Photoredox Reactions of Selected Aromatic Carbonyl Compounds. *Acc. Chem. Res.* **2019**, *52*, 726-737.

27. Ting, S.I.; Garakyaraghi, S.; Taliaferro, C.M.; Shields, B.J.; Scholes, G.D.; Castellano, F.N.; Doyle, A.G. [3]d-d Excited States of Ni(II) Complexes Relevant to Photoredox Catalysis: Spectroscopic Identification and Mechanistic Implications. *J. Am. Chem. Soc.* **2020**, *142*, 5800-5810.

28. Zheng, S.; Zhang, S-Q.; Saeednia, B.; Zhou, J.; Anna, J.M.; Hong, X.; Molander, G.A. Diastereoselective Olefin Amidoacylation via Photoredox PCET/Nickel-Dual Catalysis: Reaction Scope and Mechanistic Insights. *Chem. Sci.* **2020**, *11*, 4131-4137.

29. Coles, M.S.; Quach, G.; Beves, J.E.; Moore, E.G. A Photophysical Study of the Sensitization-Initiated Electron Transfer: Insights into the Mechanism of Photoredox Activity. *Angew. Chem. Int. Ed.* **2020**, *59*(24), 9522-9526.

30. Wang, K.; Lu, H.; Zhu, X.; Lin, Y.; Beard, M.C.; Yan, Y.; Chen, X. Ultrafast Reaction Mechanisms in Perovskite Based Photocatalytic C-C Coupling. *ACS Energy Lett.* **2020**, *5*, 566-571.

31. Vitaku, E.; Smith, D.T.; Njardarson, J.T. Analysis of the Structural Diversity, Substitution Patterns, and Frequency of Nitrogen Heterocycles among U.S. FDA Approved Pharmaceuticals. *J. Med. Chem.* **2014**, *57*, 10257-10274.

32. Chen, W.; Ma, L.; Paul, A.; Seidel, D. Direct α-C-H Bond Functionalization of Unprotected Cyclic Amines. *Nature Chem.* **2018**, *10*, 165-169.

33. Spangler, J.E.; Kobayashi, Y.; Verma, P.; Wang, D-H.; Yu, J-Q. α-Arylation of Saturated Azacycles and *N*-Methylamines via Palladium(II)-Catalyzed C(sp[3])-H Coupling. *J. Am. Chem. Soc.* **2015**, *137*, 11876-11879.

34. Shaw, M.H.; Shurtleff, V.W.; Terrett, J.A.; Cuthbertson, J.D.; MacMillan, D.W.C. Native Functionality in Triple Catalytic Cross-Coupling: sp[3] C-H Bonds as Latent Nucleophiles. *Science* **2016**, *352*, 1304-1308.

35. McNally, A.; Prier, C. K.; MacMillan, D. W. C. Discovery of an α-Amino C–H Arylation Reaction Using the Strategy of Accelerated Serendipity. *Science* **2011**, *334* (6059), 1114-1117.

36. Pirnot, M.T.; Rankic, D.A.; Martin, D.B.C.; MacMillan, D.W.C. Photoredox Activation for the Direct β-Arylation of Ketones and Aldehydes. *Science* **2013**, *339*, 1593-1596.

37. Noble, A.; MacMillan, D.W.C. Photoredox α-Vinylation of α-Amino Acids and N-Aryl Amines. *J. Am. Chem. Soc.* **2014**, *136*, 11602-11605.

38. Qvortrup, K.; Rankic, D.A.; MacMillan, D.W.C. A General Strategy for Organocatalytic Activation of C–H Bonds via Photoredox Catalysis: Direct Arylation of Benzylic Ethers. *J. Am. Chem. Soc.* **2014**, *136*, 626-629.

39. Zuo, Z.; Ahneman, D.T.; Chu, L.; Terret, J.A.; Doyle, A.G.; MacMillan, D.W.C. Merging Photoredox with Nickel Catalysis: Coupling of α-carboxyl sp[3]-carbons with Aryl Halides. *Science* **2014**, *345*, 437-440.

40. Jin, J.; MacMillan, D.W.C. Direct α-Arylation of Ethers through the Combination of Photoredox-Mediated C-H Functionalization and Minisci Reaction. *Angew. Chem. Int. Ed.* **2015**, *54*, 1565-1569.

41. Ahneman, D.T.; Doyle, A.G. C-H Functionalization of Amines with Aryl Halides by Nickel-Photoredox Catalysis. *Chem. Sci.* **2016**, *7*, 7002-7006.

42. Heitz, D.R.; Tellis, J.C.; Molander, G.A. Photochemical Nickel-Catalyzed C–H Arylation: Synthetic Scope and Mechanistic Investigations. *J. Am. Chem. Soc.* **2016**, *138*, 12715-12718.

43. Ide, T.; Barham, J.P.; Fujita, M.; Kawato, Y.; Egami, H.; Hamashima, Y. Regio- and Chemoselective Csp[3]-H Arylation of Benzylamines by Single Electron Transfer/Hydrogen Atom Transfer Synergistic Catalysis. *Chem. Sci.* **2018**, *9*, 8453-8460.

44. Revathi, L.; Ravindar, L.; Fang, W-Y.; Rakesh, K.P.; Qin, H-L. Visible Light-Induced C-H Bond Functionalization: A Critical Review. *Adv. Synth. Catal.* **2018**, *360*, 4652-4698.

45. Ma, Y.; Yao, X.; Zhang, L.; Ni, P.; Cheng, R.; Ye, J. Direct Arylation of α-Amino C(sp[3])-H Bonds by Convergent Paired Electrolysis. *Angew. Chem. Int. Ed.* **2019**, *58,* 16548-16552.

46. Walker, M. M.; Koronkiewicz, B.; Chen, S.; Houk, K. N.; Mayer, J.; Ellman, J. A. Highly Diastereoselective Functionalization of Piperidines by Photoredox-Catalyzed α-Amino C-H Arylation and Epimerization. *J. Am. Chem. Soc.* **2020**, *142*, 8194-8202.

47. Rimshaw, A.; Grieco, C.; Asbury, J.B. Note: Using Fast Digitizer Acquisition and Flexible Resolution to Enhance Noise Cancellation for High Performance Nanosecond Transient Absorbance Spectroscopy. *Rev. Sci. Instrum.* **2015**, *86*, 066107-1-066107-3.

48. Dethe, D. H.; Srivastava, A.; Dherange, B. D.; Kumar, B. V. Unsymmetrical Disulfide Synthesis through Photoredox Catalysis. *Adv. Synth. Catal.* **2018**, *360*, 3020-3025.

49. Xu, W.; Wang, W.; Liu, T.; Xie, J.; Zhu, C. Late-stage trifluoromethylthiolation of benzylic C-H bonds. *Nature Comm.* **2019**, *10*, 1-8.

50. Lei, Z.; Banerjee, A.; Kusevska, E.; Rizzo, E.; Liu, P.; Ngai, M-Y; β-Selective Aroylation of Activated Alkenes by Photoredox Catalysis. *Angew. Chem. Int. Ed.* **2019**, *58*(22), 7318-7323.

51. Yildiz, A.; Sertel, M.; Gambert, R.; Baumgärtel, H. On the Stabilities of the Anion Radicals, Dianions, and Dimerdianions of Benzenedicarbonitriles. *Electrochim. Acta.* **1988**, *33*, 169-170.

52. van den Bosch, A.; Stienlet, D.; Ceulemans, J. Spectroscopic Characterization of Alkane Radical Cations − I. Electron Absorption Spectra of 3-Methylalkane Radical Cations. *Radiat. Phys. Chem.* **1989**, *33*, 371-379.

53. Ichikawa, T.; Ota, N. ESR and Electronic Spectra of Alkane Radical Cations Formed in γ-Irradiated 3-Methylpentane and 3-Methylhexane Glasses Containing Alkane Solutes. *J. Phys. Chem.* **1987**, *91*, 3244-3248.